Novel iron complexes bearing N6-substituted adenosine derivatives: Synthesis, magnetic, [57]Fe Mössbauer, DFT, and in vitro cytotoxicity studies

Zdeněk Trávníček [a,*], Jiří Mikulík [a], Michal Čajan [a], Radek Zbořil [b], Igor Popa [a,c]

[a] *Department of Inorganic Chemistry, Faculty of Science, Palacký University, Křížkovského 10, CZ-771 47, Olomouc, Czech Republic*
[b] *Department of Physical Chemistry, Faculty of Science, Palacký University, Tř. Svobody 8, CZ-771 46, Olomouc, Czech Republic*
[c] *Laboratory of Growth Regulators, Palacký University & Institute of Experimental Botany AS CR, Šlechtitelů 11, CZ-783 71, Olomouc, Czech Republic*

ARTICLE INFO

ABSTRACT

Iron complexes (**1–7**) involving N6-benzyladenosine derivatives of the predominant composition $[Fe(L_n)Cl_3] \cdot H_2O$ {where L_1 = N6-(2-fluorobenzyl)adenosine (**1**), L_2 = N6-(4-fluorobenzyl)adenosine (**2**), L_3 = N6-(2-trifluoromethylbenzyl)adenosine (**3**), L_4 = N6-(3-trifluoromethylbenzyl)adenosine (**4**), L_5 = N6-(4-trifluoromethylbenzyl)adenosine (**5**), L_6 = N6-(4-trifluoromethoxybenzyl)adenosine (**6**), and L_7 = N6-(4-chlorobenzyl)adenosine (**7**)} have been synthesized. The compounds have been characterized by elemental analysis, variable-temperature and in-field [57]Fe Mössbauer, ES+ MS, FTIR, ^{1}H and ^{13}C NMR spectroscopies, magnetochemical and conductivity measurements, thermal (TGA/DSC/DTA) analyses, and DFT calculations. It has been found that the organic molecule is coordinated to iron via N7 atom of the appropriate adenosine derivative and the products are represented by mixtures of complexes with various iron oxidation (Fe^{III}/Fe^{II}) and spin states (S = 5/2, 4/2, 3/2, 2/2) and geometries (tetrahedral or trigonal bipyramidal). It is caused by the fact that partial redox processes proceed during the reactions due to the presence of a ribose moiety, which is oxidized to the corresponding 5′-ribotic acid, and simultaneously, a portion of Fe^{III} cations is reduced to Fe^{II} ones. Moreover, a significant effect of crystal water molecules on stereochemistry, and hence, on magnetic and spectral properties of the prepared complexes has been found. The compounds have been tested for their in vitro cytotoxicity against the following human cancer cell lines: malignant melanoma (*G-361*), osteogenic sarcoma (*HOS*), chronic myelogenous leukemia (*K-562*), and breast adenocarcinoma (*MCF-7*). The most important results have been obtained for complex **2** with IC_{50} values 8–16 μM against *HOS*, *K-562*, and *MCF-7* cell lines, and for complex **6** with IC_{50} value 4 μM against *MCF-7* cell line.

1. Introduction

The organic compounds derived from 6-benzylaminopurines (Bap), belonging to a group of plant growth hormones – called cytokinins, have been intensively studied since the 1960s. The cytokinins represent a group of compounds, which can significantly affect some of physiological functions, for example, plant cells division and senescence.[1] Moreover, a suitable substitution on the 6-benzylaminopurine skeleton can significantly influence biological function and utilization of these compounds. For that reason, many types of derivatives have been prepared and studied up to now. Among them, 2,9-disubstituted derivatives of Bap have been found to be the most interesting due to their ability to inhibit cyclin-dependent kinases (CDKs), that is, enzymes playing crucial role in the cell cycle regulation. Some of these synthetically acquired CDK inhibitors {such as *Olomoucine* = 6-(benzylamino)-2-[(2-hydroxyethyl)amino]-9-methylpurine, *Bohemine* = 6-(benzylamino)-2-[(2-hydroxypropyl)amino]-9-isopropylpurine and *Roscovitine* = 6-(benzylamino)2-[(2-hydroxymethylpropyl)amino]-9-isopropyl-purine} demonstrated considerable both in vitro and in vivo cytotoxicity against some human cancer cell lines, corresponding to their activities as CDK inhibitors.[2] For instance, Cyclacel Pharmaceuticals, Inc. announced in June 2006 that *Roscovitine* (named Seliciclib, CYC202) entered a Phase IIb of clinical trials for evaluation of the efficacy and safety of the investigated drug for previously treated non-small cell lung cancer [www.cyclacel.com].

A few years ago, we have found that the cytotoxicity may be increased after the coordination of the above-mentioned organic substances, that is both cytokinins and CDK inhibitors, to a suitable transition metal ion (e.g. Pt^{II}, Pd^{II}, Fe^{III}, and Co^{II}, Cu^{II}, Ni^{II}).[3–6] Due to undesirable side-effects of platinum-containing drugs used worldwide in cancer chemotherapy at present (i.e. *cisplatin, oxaliplatin* or *carboplatin*), the present efforts of chemists are focused on the preparation of such transition metal complexes which would be more effective and much less toxic than the above-mentioned Pt^{II}-involving drugs. Among transition metal complexes, which could meet these requirements, iron complexes bearing CDK

* Corresponding author. Tel.: +420 58 563 4944; fax: +420 58 563 4954.
  E-mail address: zdenek.travnicek@upol.cz (Z. Trávníček).

inhibitors derived from 6-benzylaminopurine could be assigned in our opinion. Searching within scientific literature databases, only few complexes or adducts of Fe$^{II/III}$ with purine or adenosine derivatives have been prepared up to now. For instance, Fe$_2$(ad)(adH)$_3$Cl$_3 \cdot$2H$_2$O {adH = adenine},[7] Fe$_2$(ado)(ClO$_4$)$_6 \cdot$4H$_2$O and Fe(ado)(ClO$_4$)$_2 \cdot$2H$_2$O {ado = adenosine},[8] [Fe(imp)(H$_2$O)$_5$]·2H$_2$O {impH$_2$ = inosine-5-monophosphate}.[9] Moreover, other N-donor aromatic and aliphatic heterocycles have been used as ligands for the syntheses of iron complexes, for example, [Fe(pyO)$_4$Cl$_2$][Fe^{I}Cl$_4$] and [Fe(pyO)$_6$](ClO$_4$)$_3$ {pyO = pyridine N-oxide derivatives},[10] [Fe(gua)Cl]·2H$_2$O {guaH = guanine},[11] Fe(xa)(xaH)$_2$(ClO$_4$)·H$_2$O and Fe(xa)$_2$(xaH)$_2$(ClO$_4$)·H$_2$O {xaH = xanthine},[12] [Fe(thf)$_4$(H$_2$O)$_2$](ClO$_4$)$_3$ {thp = tetrahydrofurane},[13] and Fe(tc)$_2$(ClO$_4$)$_2$ and Fe(tc)$_2$(ClO$_4$)$_3$ {tc = tetracycline}.[14] While chemical features and physical properties of these mentioned iron complexes were described appropriately, their potential biological activity has never been discussed yet. Recently, two ionic pair complexes of the composition (H$^+$HL)$_2$[FeCl$_5$]·2H$_2$O and (H$^+$HL)$_2$[FeCl$_5$]·3H$_2$O (HL = *Bohemine*) have been prepared, characterized, and their in vitro cytotoxicity has been evaluated.[3] Surprisingly, only three X-ray structures of iron-coordinated purine derivatives and involving Fe–purine moiety have been determined and deposited within the Cambridge Crystallographic Data Centre up to now:[15] [Fe(imp)(H$_2$O)$_5$]·2H$_2$O,[9] [Fe(gmp)(H$_2$O)$_5$]·3H$_2$O (gmpH$_2$ = guanosine-5′-monophosphate)[16] and [Fe(mp)$_3$][FeCl$_4$]Cl (mp = 6-mercaptopurine).[17]

Herein, we report the synthesis, characterization, using a broad spectrum of physico-chemical techniques, and in vitro cytotoxicity testing results of a series of high-spin Fe^{III}/Fe^{II} complexes involving differently substituted N6-benzyladenosine derivatives (see Scheme 1) of a general composition [Fe(*L*$_n$)Cl$_3$]·H$_2$O.

2. Experimental

2.1. Materials

FeCl$_3 \cdot$6H$_2$O, 6-chloro-9-riboside-purine, 4-chlorobenzylamine, 2-fluorobenzylamine, 4-fluorobenzylamine, 2-(trifluoromethyl)-

benzylamine, 3-(trifluoromethyl)benzylamine, 4-(trifluoromethyl)benzylamine, 4-(trifluoromethoxy)benzylamine, 1,10-phenanthroline, phosphoric acid, L-ascorbic acid, murexide, and solvents used were purchased from Fluka Co., or Aldrich co. and used without further purification.

2.2. Methods

IR spectra were measured on a FT-IR Nexus 670 spectrometer (ThermoNicolet) using polyethylene discs in the region of 150–600 cm^{-1} and using KBr discs in the region of 400–4000 cm^{-1}. The transmission ^{57}Fe Mössbauer spectra of all complexes were measured at 300 K in zero applied magnetic field using a Mössbauer spectrometer working in constant acceleration mode with a ^{57}Co(Rh) radioactive source. The iron foil was used as a calibration standard. The complex **6** was investigated also at 2 K in a zero external field and in an external field of 7 T applied parallel to the gamma-ray propagation. ^{1}H and ^{13}C NMR spectra of organic ligands L$_n$ and all complexes were measured in various deuterated solvents (i.e. DMSO-d_6, DMFA-d_7, methanol-d_3, and acetone-d_6) on an Avance 300 MHz NMR spectrometer (Bruker), with an inverse probe used. ES+ mass spectra were recorded using a flow injection mode on the Waters ZMD 2000 mass spectrometer. The mass-monitoring interval was 40–1300 m/z. The spectra were collected by using 3.0 s cyclical scans and by applying the sample cone voltage 20, 40 or 60 V and capillary voltage +3.0 kV, at the source block temperature 100 °C, desolvation temperature 250 °C, cone gas flow rate 50 l h^{-1} and desolvation gas flow rate 500 l h^{-1}. The mass spectrometer was directly coupled to a MassLynx data system. Elemental analyses (C, H, N) were carried out on a Flash EA 1112 CHN(O) analyzer (ThermoFinnigan), the iron contents were estimated by chelatometric titration (with murexide as an indicator). UV–Vis spectrometer Lambda40 (Perkin–Elmer) was used for the determination of a Fe^{III}/Fe^{II} ratio in the complexes by using the method described in the literature.[18] The magnetic susceptibility measurements were carried out for all compounds by using the Faraday method at 298 K with Hg[Co(SCN)$_4$] as a cal-
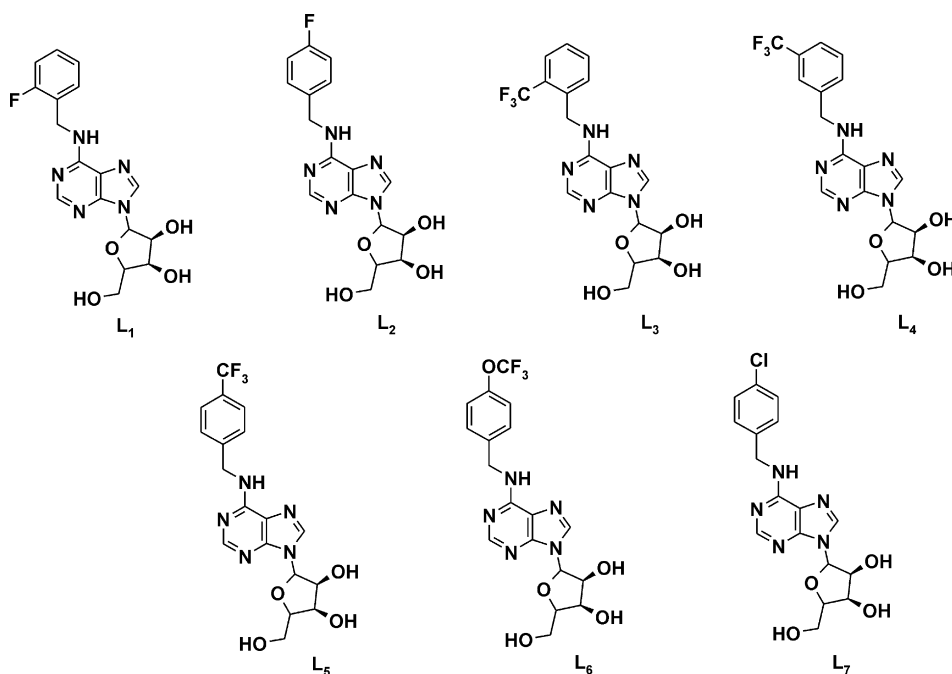
Scheme 1. N6-(benzyl)adenosine derivatives used as ligands in this study.

ibrant. Magnetic properties of the compounds **2**, **4** and **6** were also studied in the temperature range of 80–300 K. The molar susceptibilities were corrected for diamagnetism using Pascal's constants.[19] Conductivity measurements were performed on a Cond340i/SET Conductivity Meter (WTW, Germany) at 25 °C using 10^{-3} mol dm^{-3} acetone solutions.[20] TGA/DSC analyses were performed on a TGA/DSC XP-10 Thermogravimetric Analyzer (THASS) in the temperature range of 20–1000 °C with temperature gradient of 5 °C min^{-1}, DSC analyses were performed in the temperature range of 20–400 °C with temperature gradient of 5 °C min^{-1}. DTA analysis of complex **6** was performed with a TGA/DTA 6200 Exstar thermal analyzer with a sample weight of 12.2 mg and thermal gradient of 5 °C min^{-1}. All thermogravimetric measurements were carried out in air atmosphere.

2.3. Biological activity testing

Human malignant melanoma cell line *G-361*, human osteogenic sarcoma cell line *HOS*, human chronic myelogenous leukemia cell line *K-562*, and human breast adenocarcinoma cell line *MCF-7* were used for vitro cytotoxicity testing of the synthesized compounds by a calcein acetoxymethyl (AM) assay. The tumor cells were maintained in plastic tissue culture flasks and grown on Dulbecco's modified Eagle's cell culture medium (DMEM) at 37 °C in 5% CO$_2$ atmosphere and 100% humidity. The cell suspension of approximate density 1.25×105 cells ml^{-1} was reattributed into 96-well microtitre plates (Nunc, Denmark). After 12 h of preincubation, the tested compounds (in the 0.5–200 and 0.5–50 μM range, respectively) were added. The incubation lasted for 72 h. At the end of this period, the cells were incubated for 1 h with calcein AM, and the fluorescence of the live cells was measured at 485/538 nm (ex/em) with a Fluoroskan Ascent (Labsystems, Finland). IC$_{50}$ values, the drug concentration lethal to 50% of tumor cells, were estimated. The presented values are represented by arithmetic means determined from three values. The deviations from the arithmetic mean values not exceed 20%.

2.4. Preparation of organic ligands L$_1$–L$_7$

All N6-(benzyl)adenosine derivatives (L$_1$–L$_7$) have been synthesized according to the published procedure (see Scheme 2).[21] One millimole of 6-chloro-9-riboside-purine and 4/3 mmol of the appropriate substituted benzylamine, that is, 2-(fluoro)benzylamine for L$_1$, 4-(fluoro)benzylamine for L$_2$, 2-(trifluoromethyl)benzylamine for L$_3$, 3-(trifluoromethyl)benzylamine for L$_4$, 4-(trifluoromethyl)benzylamine for L$_5$, 4-(trifluoromethoxy)benzylamine for L$_6$, and 4-(chloro)-benzylamine for L$_7$, were dissolved in 20 ml of butanol in an ultrasonic bath. Then, triethylamine was added dropwise while stirring the reaction mixture. The mixture was heated up to 90 °C and stirred for 4 h. Then, after slow cooling, the solution was put into the freezer. After 12 h, the white solid was filtered off,

washed with a small amount of cold butanol, several times by a small amount of cold distilled water, and finally by diethyl ether. The product was recrystallized from ethanol and its composition and purity were proved by HPLC, elemental analysis, and thin-layer chromatography (TLC).

L$_1$: Yield: ∼90%. Anal. Calcd for C$_{17}$H$_{17}$N$_5$O$_4$F$_1$: C, 54.5; N, 18.7; H, 4.6. Found: C, 54.7; N, 18.8; H, 4.6%. TLC: one spot. **L$_2$**: Yield: ∼85%. Anal. Calcd for C$_{17}$H$_{17}$N$_5$O$_4$F$_1$: C, 54.5; N, 18.7; H, 4.6. Found: C, 54.3; N, 18.9; H, 4.7%. TLC: one spot. **L$_3$**: Yield: ∼95%. Anal. Calcd for C$_{18}$H$_{17}$N$_5$O$_4$F$_3$: C, 50.9; N, 16.5; H, 4.0. Found: C, 51.1; N, 16.5; H, 3.9%. TLC: one spot. **L$_4$**: Yield: ∼85%. Anal. Calcd for C$_{18}$H$_{17}$N$_5$O$_4$F$_3$: C, 50.9; N, 16.5; H, 4.0. Found: C, 51.0; N, 16.8; H, 4.0%. TLC: one spot. **L$_5$**: Yield: ∼90%. Anal. Calcd for C$_{18}$H$_{17}$N$_5$O$_4$F$_3$: C, 50.9; N, 16.5; H, 4.0. Found: C, 51.0; N, 16.6; H, 4.1%. TLC: one spot. **L$_6$**: Yield: ∼85%. Anal. Calcd for C$_{18}$H$_{17}$N$_5$O$_5$F$_3$: C, 49.1; N, 15.9; H, 3.9. Found: C, 49.2; N, 15.7; H, 4.0%. TLC: one spot. **L$_7$**: Yield: ∼85%. Anal. Calcd for C$_{17}$H$_{17}$N$_5$O$_4$Cl$_1$: C, 52.2; N, 17.9; H, 4.4. Found: C, 52.1; N, 17.7; H, 4.4%. TLC: one spot.

2.5. General preparation of the complexes (1–7)

A total amount of 1 mmol of the corresponding organic ligand {i.e., N6-(2-fluorobenzyl)adenosine, N6-(4-fluorobenzyl)adenosine, N6-(2-trifluoromethylbenzyl)ade-nosine, N6-(3-trifluoromethylbenzyl)adenosine, N6-(4-tri-fluoromethylbenzyl)adenosine, N6-(4-trifluoromethoxybenzyl)adenosine, and N6-(4-chlorobenzyl)adenosine} was dissolved in ethanol (30 ml) and added to an ethanolic solution (15 ml) of FeCl$_3$·6 H$_2$O (1 mmol, 270 mg). The reaction mixture was stirred at 65 °C for 3–4 h. Then, the mixture was cooled down to room temperature and the orange–brown solid formed. It was filtered off, washed several times with a small amount of diethylether, and dried in a vacuum desiccator over P$_4$O$_{10}$.

In quest to optimize reaction conditions and pathways regarding the preparation of Fe-complexes, we performed many experiments during which we changed the type of iron-containing inorganic salts, molar ratio of reactants, temperature, and solvents. Herein, we present the results which were obtained by the way described above. In the case that we used Fe(NO$_3$)$_3$·9H$_2$O, Fe(ClO$_4$)$_3$·xH$_2$O, FeSO$_4$·7H$_2$O or Fe(ClO$_4$)$_2$·xH$_2$O as a starting material, and changed molar ratios of the reactants, we obtained mixtures of the appropriate iron-containing salt and free ligand, and Fe$^{II/III}$-complexes. That is why the above-described procedure, leading to the preparation of the discussed Fe-complexes only, can be considered as the optimized one.

(**1**): Yield: ∼50%. Anal. Calcd for C$_{17}$H$_{18}$N$_5$O$_4$Fe$_1$Cl$_3$F$_1$: C, 37.9; N, 13.0; H, 3.4; Fe, 10.4. Found: C, 37.7; N, 12.8; H, 3.8; Fe, 10.7%. IR (cm^{-1}): 3401w, 3250w, 3113w, 2975w, 2927w, 2839w, 1655vs, 1616s, 1586m, 1491m, 1455s, 1402m, 1349m, 1313w, 1276w, 1229m, 1181w, 1123m, 1093s, 1035m, 913w, 872w, 832w, 760m, 657w, 639w, 614w, 559w, 533w, 436w. ES+ MS (*m/z*): 377 [L$_1$]$^+$,
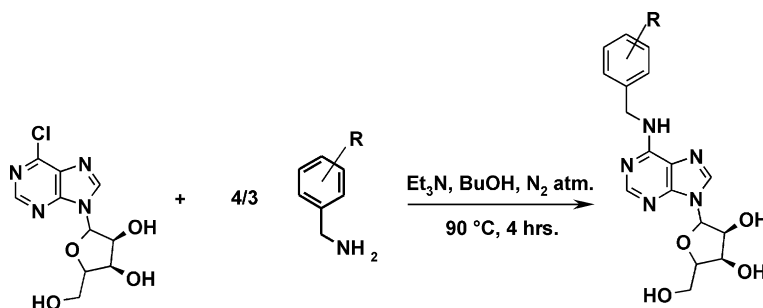
Scheme 2. A general pathway for the synthesis of organic ligands used for the preparation of complexes (**1–7**).

244 [L_1–ribose]$^+$. (**2**): Yield: 55%. Anal. Calcd for $C_{17}H_{20}N_5O_5$-$Fe_1Cl_3F_1$: C, 36.8; N, 12.6; H, 3.6; Fe, 10.1. Found: C, 37.2; N, 12.2; H, 3.6; Fe, 10.2%. IR (cm^{-1}): 3382w, 3352w, 3101w, 2929w, 1657vs, 1604s, 1510s, 1452m, 1433m, 1416m, 1403m, 1343m, 1279w, 1221s, 1158m, 1119m, 1094s, 1081s, 1015m, 909w, 893w, 825m, 778w, 743w, 638w, 612w, 561w, 532w, 510w, 483w, 445w. ES+ MS (m/z): 377 [L_2]$^+$, 244 [L_2–ribose]$^+$. (**3**): Yield: ~85%. Anal. Calcd for $C_{18}H_{20}N_5O_5Fe_1Cl_3F_4$: C, 35.7; N, 11.5; H, 3.3; Fe, 8.9. Found: C, 35.8; N, 11.4; H, 3.4; Fe, 9.2%. IR (cm^{-1}): 3414w, 3256w, 3088w, 2929w, 1645vs, 1506w, 1454m, 1426m, 1405m, 1365w, 1315vs, 1218w, 1168m, 1117s, 1059m, 1038m, 909w, 827w, 822w, 771m, 743w, 717w, 625w, 599w, 536w. ES+ MS (m/z): 426 [L_3]$^+$, 294 [L_3–ribose]$^+$. (**4**): Yield: 70%. Anal. Calcd for $C_{18}H_{18}N_5O_4Fe_1Cl_3F_4$: C, 36.8; N, 11.9; H, 3.1; Fe, 9.2. Found: C, 36.5; N, 11.6; H, 3.3; Fe, 9.3%. IR (cm^{-1}): 3292w, 2934w, 1667vs, 1646vs, 1542w, 1506w, 1451m, 1405m, 1328vs, 1201m, 1166s, 1124vs, 1098s, 1074s, 902w, 871w, 802w, 779w, 750w, 702m, 659w, 640w, 611w, 568w, 534w, 505w, 456w. ES+ MS (m/z): 426

[L_4]$^+$, 294 [L_4–ribose]$^+$. (**5**): Yield: ~70%. Anal. Calcd for $C_{18}H_{20}N_5O_5$-$Fe_1Cl_3F_4$: C, 35.7; N, 11.6; H, 3.3; Fe, 8.9. Found: C, 35.5; N, 11.8; H, 3.3; Fe, 9.1. IR (cm^{-1}): 3250w, 3142w, 2925w, 1923w, 1657vs, 1619s, 1580m, 1510m, 1451m, 1418s, 1403m, 1326vs, 1281m, 1212m, 1165s, 1123s, 1066vs, 1018m, 913w, 888w, 864w, 820m, 778m, 637w, 611m, 592w, 537w, 493w. ES+ MS (m/z): 426 [L_5]$^+$, 294 [L_5–ribose]$^+$. (**6**): Yield: ~90%. Anal. Calcd for $C_{18}H_{20}N_5O_6$-$Fe_1Cl_3F_4$: C, 34.8; N, 11.3; H, 3.2; Fe, 8.7. Found: C, 34.8; N, 11.6; H, 3.2; Fe, 9.0%. IR (cm^{-1}): 3408w, 3241w, 3114w, 2934w, 1657vs, 1615m, 1510m, 1452m, 1419m, 1404m, 1347w, 1263vs, 1220s, 1165m, 1122m, 1106m, 1081m, 1019w, 919w, 890w, 814w, 778w, 744w, 606w, 556w, 530w, 423m. ES+ MS (m/z): 441 [L_6]$^+$, 309 [L_6–ribose]$^+$. (**7**): Yield: ~65%. *Anal.* Calc. for $C_{18}H_{20}N_5O_5$-Fe_1Cl_4: C, 35.5 (35.7); N, 12.1 (12.2); H, 3.8 (3.5); Fe, 9.7 (9.6). Found: C, 35.5; N, 12.1; H, 3.8; Fe, 9.7%. IR (cm^{-1}): 3408w, 3249w, 3198w, 3113w, 2975w, 2921w, 2847w, 1656vs, 1615m, 1576m, 1491m, 1448m, 1403m, 1342m, 1278w, 1209m, 1123m, 1089m, 1041m, 1014m, 917w, 885w, 801w, 777w, 723w, 637w, 611w, 557w, 531w, 486w. ES+ MS (m/z): 392 [L_7]$^+$, 260 [L_7–ribose]$^+$.

3. Results and discussion

3.1. General features

The reaction between $FeCl_3 \cdot 6H_2O$ and a substituted N6-benzyl-adenosine (in a molar ratio of 1:1) in ethanol gave complexes of a general formula [$Fe(L_n)Cl_3$] $\cdot H_2O$. Chemical composition, magnetic and conductivity data of the complexes are given in Table 1. All prepared compounds are hygroscopic and they need to be stored in vacuum desiccator over P_4O_{10} or NaOH as a drying medium.

Table 1
Composition, magnetic, and conductivity data for the complexes

Complex	μ_{eff}/μ_B	λ_M[a] (S cm^2 mol^{-1})
[Fe(L_1)Cl$_3$]·H$_2$O (**1**)	5.32	4.2
[Fe(L_2)Cl$_3$]·H$_2$O (**2**)	5.40	5.3
[Fe(L_3)Cl$_3$]·H$_2$O (**3**)	5.56	5.3
[Fe(L_4)Cl$_3$]·H$_2$O (**4**)	5.45	11.9
[Fe(L_5)Cl$_3$]·H$_2$O (**5**)	5.32	6.0
[Fe(L_6)Cl$_3$]·H$_2$O (**6**)	5.44	5.4
[Fe(L_7)Cl$_3$]·H$_2$O (**7**)	5.42	9.7

[a] Measured in acetone.

Table 2
^{57}Fe Mössbauer spectral data of complexes **1–7**

Compound	Component	T (K)	δ (mm s^{-1})	ΔE_Q (mm s^{-1})	Γ (mm s^{-1})	RA (%)	Assignment
1	Doublet	300	0.33	0.68	0.68	46	Fe^{III}(HS, TB)
	Singlet		0.24	—	0.30	17	Fe^{III}(HS, T$_d$)
	Doublet		1.24	2.48	0.31	15	Fe^{II}(HS, TB)
	Doublet		1.04	2.10	0.45	22	Fe^{II}(HS, T$_d$)
2	Doublet	300	0.33	0.71	0.57	80	Fe^{III}(HS, TB)
	Singlet		0.20	—	0.33	11	Fe^{III}(HS, T$_d$)
	Doublet		1.17	2.47	0.47	5	Fe^{II}(HS, TB)
	Doublet		1.06	1.95	0.49	4	Fe^{II}(HS, T$_d$)
3	Doublet	300	0.32	0.71	0.49	65	Fe^{III}(HS, TB)
	Singlet		0.24	—	0.52	14	Fe^{III}(HS, T$_d$)
	Doublet		1.29	2.32	0.41	11	Fe^{II}(HS, TB)
	Doublet		1.09	1.90	0.47	10	Fe^{II}(HS, T$_d$)
4	Doublet	300	0.35	0.69	0.47	63	Fe^{III}(HS, TB)
	Singlet		0.25	—	0.58	23	Fe^{III}(HS, T$_d$)
	Doublet		1.19	2.72	0.29	5	Fe^{II}(HS, TB)
	Doublet		1.07	2.07	0.41	9	Fe^{II}(HS, T$_d$)
5	Doublet	300	0.33	0.75	0.39	25	Fe^{III}(HS, TB)
	Singlet		0.25	—	0.64	57	Fe^{III}(HS, T$_d$)
	Doublet		1.21	2.51	0.39	12	Fe^{II}(HS, TB)
	Doublet		1.03	1.96	0.25	6	Fe^{II}(HS, T$_d$)
6	Doublet	300	0.32	0.72	0.44	40	Fe^{III}(HS, TB)
	Singlet		0.25	—	0.58	42	Fe^{III}(HS, T$_d$)
	Doublet		1.19	2.44	0.43	12	Fe^{II}(HS, TB)
	Doublet		1.02	2.00	0.32	6	Fe^{II}(HS, T$_d$)
	Doublet	2	0.44	0.50	0.48	42	Fe^{III}(HS, TB)
	Singlet		0.37	—	0.55	36	Fe^{III}(HS, T$_d$)
	Doublet		1.30	1.76	0.47	9	Fe^{II}(HS, TB)
	Doublet		1.14	1.26	0.36	13	Fe^{II}(HS, T$_d$)
7	Doublet	300	0.34	0.70	0.49	30	Fe^{III}(HS, TB)
	Singlet		0.25	—	0.58	45	Fe^{III}(HS, T$_d$)
	Doublet		1.30	2.40	0.26	9	Fe^{II}(HS, TB)
	Doublet		1.12	2.07	0.39	16	Fe^{II}(HS, T$_d$)

δ, isomer shift related to metallic iron (±0.01 mm s^{-1}); ΔE_Q, quadrupole splitting (±0.01 mm s^{-1}); Γ, full width of spectral line at a half maximum (±0.01 mm s^{-1}); RA, relative spectrum area (±1%); HS, high-spin; TB, trigonal-bipyramidal arrangement; T_d, tetrahedral arrangement.

The complexes are soluble in *N,N*-dimethylformamide (DMFA) and acetone, partially soluble in methanol and ethanol, and nearly insoluble in CHCl$_3$ and diethylether. Based on results following from magnetic, UV/Vis spectral, and mainly from Mössbauer data, a portion of Fe^{III} cations was reduced to Fe^{II} during the synthesis due to reduction abilities of the ribose molecule, which is attached to an adenine moiety via N9 nitrogen atom. We have reason to believe that the ribose was oxidized to the corresponding 5′-ribotic acid. The fact that the Fe^{III} reduction proceeded during the synthetic pathway was supported by a simple UV/Vis spectral measurement.[18] The conclusion regarding the reduction process of Fe^{III} to Fe^{II} was proved unambiguously by ^{57}Fe Mössbauer spectroscopy (see below). As expected, the conductivity data in acetone illustrated non-ionic features of the compounds in the solvent used (see Table 1).[20]

3.2. ^{57}Fe Mössbauer spectroscopy and magnetic measurements

Mössbauer parameters obtained for all the complexes at room temperature, and for complex **6** also at 2 K, are given in Table 2.
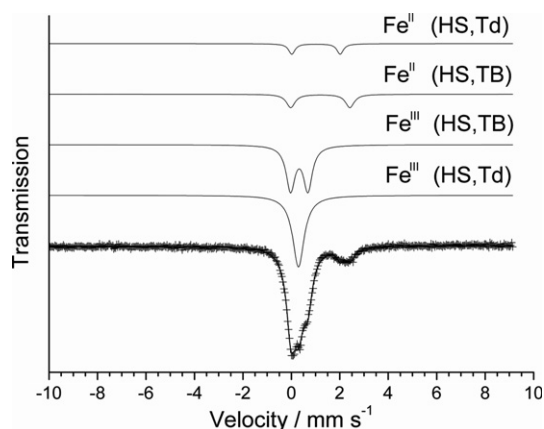

Figure 1. ^{57}Fe Mössbauer spectrum of complex **6** measured at room temperature including the fitted subspectra and assigned states of iron (HS, high-spin; T_d, tetrahedron; TB, trigonal-bipyramid).

Generally, Mössbauer spectra are very similar and consist of four subspectra reflecting the presence of four non-equivalent structural, oxidation, and/or spin states of iron cations in the samples. Figure 1 shows the representative room temperature Mössbauer spectrum of the complex **6** including its mathematical deconvolution. The suggested stereochemical arrangements, valence, and spin states of the iron ions were assigned to individual subspectra mainly on the basis of interpretation of their hyperfine parameters supported by magnetic data and DFT calculations (see below). These four possible different arrangements are depicted in Figure 2. Following the isomer shift (δ) values derived for individual subspectra at room temperature (see **Table 2**), there may be two clearly identified high-spin Fe^{III} components in all samples. Singlets with the lowest δ values (0.20–0.25 mm s^{-1}) and zero quadrupole splitting (ΔE_Q) would be assigned to tetrahedral (T_d) high-spin Fe^{III} ($S = 5/2$). Doublets with higher isomer shifts (0.32–0.35 mm s^{-1}) and ΔE_Q (0.68–0.75 mm s^{-1}) parameters indicate a presence of the Fe^{III} species with the higher coordination number accompanied by decrease in symmetry of the electric charge distribution in the vicinity of the central ion. These doublet components may be connected with a distorted trigonal-bipyramidal (D_{3h}) or distorted square-pyramidal (D_{4v}) Fe^{III} arrangement with $S = 3/2$. It is worthy to emphasize that these trivalent iron species predominate in the samples as deduced from their total spectral areas ranging between 63% and 91% (see Table 2). Nevertheless, all the spectra exhibit two other subspectra with similar δ values (1.17–1.30 and 1.03–1.20 mm s^{-1}), but distinct ΔE_Q values (2.40–2.72 and 1.90–2.10 mm s^{-1}, respectively). They are ascribable to Fe^{II} ions formed from their Fe^{III} counterparts during the synthetic procedure due to the reduction effect of the ribose molecule. The doublets with the lower quadrupole splitting parameters probably originate from a tetrahedral high-spin ($S = 4/2$) Fe^{II} component, while the next ones with higher ΔE_Q may be assigned to a distorted trigonal-bipyramidal or square-pyramidal ($S = 2/2$) Fe^{II} component. Both Fe^{II} tetrahedral and Fe^{II} trigonal-bipyramidal species are in minority, which did not exceed 37% overall. For that reason, effective magnetic moment values, as presented in Table 1, were not influenced significantly as compared to a spin only value typical for five unpaired electrons in tetrahedral Fe^{III} complexes ($S = 5/2$). In quest to find more information on the structural and magnetic
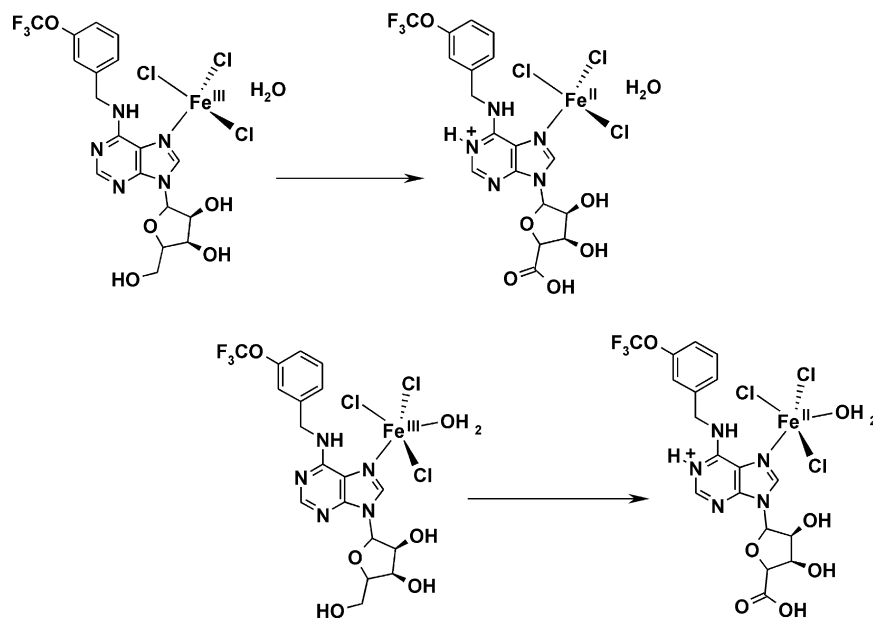

Figure 2. Possible geometrical arrangements and compositions of the complex **6**, as predicted mainly on the basis of ^{57}Fe Mössbauer data.

states of iron in the studied samples, we performed the Mössbauer measurement of complex **6** at 2 K. As the key magnetic information, the sample remains paramagnetic even at such a low temperature. In addition to the temperature shift, we observed a significant decrease in the quadrupole splitting of all subspectra except for that corresponding to tetrahedral Fe^{III} ions preserving the singlet character (see Table 2). This fact provides an indirect proof for a considerable distortion of all other local Fe environments in samples at room temperature. The differences in the relative spectral areas of individual Fe species, if the room temperature and the 2 K spectra are compared, are clearly due to the different *f*-factors of non-equivalent Fe fractions.

The room temperature effective magnetic moment values of the complexes **1**–**7**, which can be seen in Table 1, vary from 5.32 to 5.59 μ_{eff}/μ_B, while the room temperature $\chi_M T$ values are as follows: 3.541 cm³ K mol⁻¹ (for **1**), 3.558 cm³ K mol⁻¹ (for **2**), 3.762 cm³ K mol⁻¹ (for **3**), 3.809 cm³ K mol⁻¹ (for **4**), 3.447 cm³ K mol⁻¹ (for **5**), 3.599 cm³ K mol⁻¹ (for **6**), and 3.578 cm³ K mol⁻¹ (for **7**). All μ_{eff}/μ_B as well as $\chi_M T$ values are significantly lower than those expected for a $S = 5/2$ spin state (a spin only value is 5.90 μ_{eff}/μ_B with $(4/g^2)\chi T = 4.377$ cm³ K mol⁻¹).[19] The reasons for the decrease in effective magnetic moment values may be the presence of the Fe^{II} species, and generally the presence of several structural arrangements in the vicinity of central atom yielding different oxidation and spin states of iron within each of the complexes as supported by Mössbauer data. In summary, the probable geometries and oxidation states, derived from Mössbauer and magnetic data, can be as follows: high-spin tetrahedral Fe^{III} ($S = 5/2$), high-spin trigonal-bipyramidal Fe^{III} ($S = 3/2$), high-spin tetrahedral Fe^{II} ($S = 4/2$), and high-spin trigonal-bipyramidal Fe^{II} ($S = 2/2$). It should be noted that such a miscellaneous spectrum of the oxidation and valence states of iron occurring in the samples is probably related not only to the above-mentioned partial reduction process, but also to a role of the water molecule in the system. The presence of the water molecule may have a significant impact on stereochemistry, and thus, on magnetic and spectral properties of the complexes depending on the fact if it acts as a ligand or is situated outside of the coordination sphere as the crystal water molecule. In the case of the water bonding as a ligand, the coordination number of iron changes from four to five. In our systems, this is accompanied by a change of geometries from tetrahedral (T_d) to trigonal-bipyramidal (D_{3h}), resulting in a decrease in spin states from $S = 5/2$ to $S = 3/2$ for Fe^{III} cations and from $S = 4/2$ to $S = 2/2$ for Fe^{II} cations. Magnetic properties of complexes **2**, **4**, and **6** have also been studied in the temperature interval of 300–80 K. The temperature dependence of μ_{eff}/μ_B and χ_M for the representative complex **2** is displayed in Figure 3. It has been found that the effective magnetic moment value is smoothly decreased together with the temperature lowering from 300 to 80 K, that is from 5.45 to 5.11 μ_{eff}/μ_B for **2**, from 5.38 to 4.99 μ_{eff}/μ_B for **4**, and from 5.59 to 5.14 μ_{eff}/μ_B for **6**. As for a general course of temperature dependence of effective magnetic moment, it shows one of the typical magnetic features of mononuclear high-spin Fe^{III} complexes.

To bring better insight into the different iron states and possible magnetic interactions among them, we also performed low-temperature (2 K) in-field (7 T) Mössbauer characterization of the representative complex **6** (Fig. 4). From such a spectrum it is obvious that the high external magnetic field induced the magnetic ordering (sextet) in the case of tetrahedral Fe^{III} and Fe^{II} components. This assignment is based on the perfect correspondence of the isomer shift parameters compared to the zero-field spectrum. Sextet corresponding to the tetrahedral Fe^{III} state ($S = 5/2$) reveals the effective magnetic field (B_{eff}) of 44 T and the zero quadrupole shift (ε_Q), proving the preservation of the maximum symmetry of the iron environment also in the magnetically ordered state (see the zero ΔE_Q in the paramagnetic singlet state – Figure 1, Table 2). The sec-
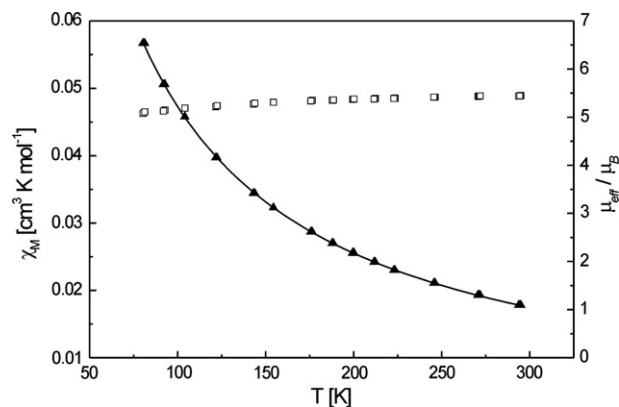

Figure 3. Temperature dependence of μ_{eff}/μ_B and χ_M for complex **2**. The continuous line represents the best-fit to the Curie–Weiss law.

ond sextet ascribed to the tetrahedral Fe^{II} component ($S = 4/2$) possesses the larger B_{eff} (46.5 T) and high negative value of ε_Q (−1.0 mm s⁻¹). A type of magnetic ordering induced by a high external magnetic field can be determined from the intensities of the 2nd and 5th lines of both sextets. In the used measuring geometry, where the external magnetic field is applied parallel to the gamma-ray propagation, the zero intensity of these lines unambiguously confirms the ferromagnetic ordering in both tetrahedral high-spin state complexes. The remaining two doublet subspectra originating from the trigonal-bipyramidal Fe components indicate the absence of any exchange interactions among these iron ions. They show almost the same isomer shift parameters as in the zero-field spectrum, however, the quadrupole shift parameters are significantly increased (1.65 mm s⁻¹ for Fe^{III} and 2.80 mm s⁻¹ for Fe^{II}), which is a probable structural response to the application of a high external magnetic field. The overall spectrum areas belonging to trivalent (79%) and divalent iron states (21%) are nearly the same as those derived from the zero-field spectrum measured at the same temperature (see Table 2). Let us conclude this part by a statement that external magnetic field induced weak ferromagnetic interactions in the framework of the tetrahedral high-spin Fe^{III} ions as well as in the framework of the tetrahedral high-spin Fe^{II} species, while the Fe^{III} and Fe^{II} ions being in the trigonal-bipyramidal arrangements remained in the paramagnetic states. An exchange between Fe^{III} and Fe^{II} ions cannot be supported from the determined Mössbauer parameters.
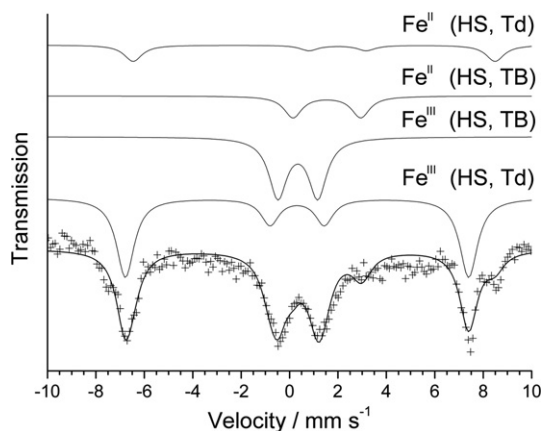

Figure 4. ⁵⁷Fe Mössbauer spectrum of complex **6** measured at 2 K in the external magnetic field of 7 T including the fitted subspectra and assigned states of iron (HS, high-spin; T_d, tetrahedron; TB, trigonal-bipyramid).

3.3. ^{1}H, ^{13}C NMR and ES+ MS spectral data

Low concentrated sample solutions were used for ^{1}H and ^{13}C NMR spectra measurements due to paramagnetism of the complexes **1**–**7**. The low concentration of the samples caused the increase in intensities of the deuterated solvent signals and decrease in intensities of some important signals of the complexes. In quest to increase quality and quantity of sample signals, the various deuterated solvents (i.e. DMSO-d_6, methanol-d_3, DMFA-d_7, and acetone-d_6) were used for NMR experiments. The best NMR results were obtained in the case of complexes **1** and **2** measured in acetone-d_6 solutions. Provided that the adenosine derivatives (L$_1$–L$_7$) are coordinated to the iron atom via N7 atom of a purine moiety, the most significant changes in coordination chemical shifts ($\Delta\delta$, where $\Delta\delta$ is defined as $\delta_{\text{complex}} - \delta_{\text{ligand}}$) should be anticipated for C8–H signal in ^{1}H NMR spectra. The experiments clearly supported this presumption with $\Delta\delta$(C8–H) values of 0.32 ppm (for **1**) and 0.39 ppm (for **2**). The remaining interpretable chemical shifts regarding any other proton signals observed in ^{1}H NMR spectra of the complexes did not differ significantly as compared to those of free adenosine derivatives (e.g. maximal $\Delta\delta$(N6–H) = 0.02 ppm for **1**, maximal $\Delta\delta$(C2–H) = 0.02 ppm for **1**, $\Delta\delta$ for O17–H, O18–H and O20–H is not greater then 0.07 ppm). These facts confirmed our assumption that adenosine derivatives cannot be coordinated through the ribose moiety to iron atom, and moreover, that the ligand cannot also be bonded to iron through N1, N3, and N6 atoms of the adenosine moiety. The most important chemical shifts were observed in ^{13}C NMR spectra of some complexes, where the greatest coordination shifts were determined for C8 and C5 atoms. Unfortunately, the interpretation of majority of ^{13}C NMR spectra could not be unambiguous due to sample paramagnetism originating from iron cation. However, we can conclude that the coordination of the organic molecule to iron proceeds via N7 atom with high probability.

ES+ mass spectra were carried out for all the complexes **1**–**7**. The spectra revealed only a few structurally important fragments. Molecular peaks belonging to organic ligands L$_n$ were observed in the spectra of all the complexes (at 376 *m/z* for **1**, **2**; at 426 *m/z* for **3**, **4**, **5**; at 441 *m/z* for **6**; and at 392 *m/z* for **7**). The peaks observed at 244 *m/z* (for **1** and **2**), 294 *m/z* (for **3**, **4** and **5**), 309 (for **6**) and 260 *m/z* (for **7**) can be attributed to fragments belonging to substituted 6-(benzylamino)purine moiety, that is to [L$_n$–ribose]$^+$.

3.4. Infrared spectroscopy

The most important IR data are summarized in the Table 3. FT IR spectra of all complexes showed peaks proving the presence of adenosine derivatives as ligands in the complexes (**1**–**7**). The spectra revealed that the maximum belonging to ν(C=N) is typically found at 1628 cm^{-1} in the case of free adenosine derivatives, which is significantly shifted to higher wave numbers in the case of the complexes ($\approx$1655 cm^{-1}). This significant shift could be used as an indirect proof of the coordination of the organic ligand via the

purine moiety to iron atom. Other important maxima, observed in the range of 1448–1455 and 1576–1604 cm^{-1} may be connected with the ν(C=C)$_{ar}$ vibration. The ν(C$_{ar}$–F) vibration appeared at 1229 cm^{-1} for complex **1** and at 1221 cm^{-1} for complex **2**. The bands observed at 3382–3414 and 3100–3250 cm^{-1} can be attributed to ν(N–H) and ν(C$_{ar}$–H) vibration, respectively.[22] However, the bands appearing within the former interval can be also assigned to ν(O–H) stretch vibration originating from water molecule. The maxima between 650 and 930 cm^{-1} are assignable to the skeletal vibrations of aromatic ring. Pure ribose IR spectrum shows, apart from others, two maxima which correspond to ν(C$_{alif}$–O) stretch vibration. The first maximum, observed at 1030 cm^{-1}, belongs to secondary aliphatic alcohol group, and the second one, at 1110 cm^{-1}, belongs to hemiacetalic bond.[22] The corresponding absorptions were found in spectra of the studied complexes in the ranges of 1035–1081 and 1074–1124 cm^{-1}, respectively. The spectra of all complexes (**1**–**7**) showed the very strong maximum at 382 cm^{-1}, which is clearly assignable to the ν(Fe–Cl) vibration.[23] The peak about 320 cm^{-1} is hard to assign, but we may assume that it can be connected with the ν(Fe–N) vibration, which is expected to be observed in this region.[24,25]

3.5. Thermal analysis

TGA and DSC analyses were carried out for all the complexes **1**–**7**, and moreover, DTA analysis was performed for complex **6**. The thermal decomposition, which is very similar for all complexes, proceeded in four main steps. Figure 5 represents TGA, DSC, and DTA curves of complex **6**. The first weight loss can be seen in the temperature range of 45–112 °C and is connected with the elimination of one water molecule (found/calcd: 2.6%/2.9%). This step is clearly supported by a broad *endo*-effect in the temperature range of 33–106 °C and with the minimum on the DSC curve at 75 °C. The activation energy value connected with the thermal effect, ΔH, is equal to 12.2 J g^{-1} ($\approx$7.6 kJ mol^{-1}, 1.8 kcal mol^{-1}). It has to be noted that the temperature interval in which the water
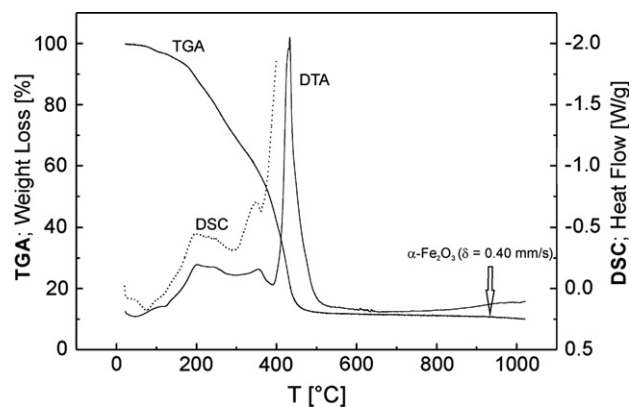

Figure 5. TGA, DTA and DSC curves of complex **6**.

Table 3
Selected IR spectral data (cm^{-1}) of the complexes (**1**–**7**) and their assignements

Compound	ν(C=N)	ν(C=C)$_{ar}$	ν(C$_{alif}$–O)	ν(C$_{ar}$–F)	ν(Fe–Cl)	ν(Fe–N)
[Fe(L$_1$)Cl$_3$]·H$_2$O (**1**)	1655vs	1586m, 1455m	1035m/1093m	1229m	382s	320w
[Fe(L$_2$)Cl$_3$]·H$_2$O (**2**)	1657vs	1604s, 1452s	1040m/1081s	1221s	382s	323w
[Fe(L$_3$)Cl$_3$]·H$_2$O (**3**)	1645vs	1610s, 1454m	1038m/1117s	–	382s	322w
[Fe(L$_4$)Cl$_3$]·H$_2$O (**4**)	1646vs	1614s, 1451m	1074s/1124s	–	382s	320w
[Fe(L$_5$)Cl$_3$]·H$_2$O (**5**)	1657vs	1580s, 1451m	1066s/1123s	–	382s	322w
[Fe(L$_6$)Cl$_3$]·H$_2$O (**6**)	1657vs	1616s, 1452m	1081m/1106m	–	383s	320m
[Fe(L$_7$)Cl$_3$]·H$_2$O (**7**)	1656vs	1576m, 1448m	1041m/1089m	–	382s	320w

molecule is leaving the sample is rather broad. This phenomenon is probably caused by the presence of unequal water molecules, where a majority portion of these molecules probably exists in the form of a crystalline water and a minority portion may be coordinated to iron atom as a ligand (see Section 3.2). Thus, the temperature interval broadening is detected as a consequence of the last-mentioned possibility. The main thermal decay proceeds within the interval of 157 and 430 °C. This weight loss is probably connected with the combination of dissociation of ribose molecule, and consequently, with thermal degradation of the remaining part of the organic molecule. This degradation is accompanied by three *exo*-effects on both DSC and DTA curves. The energy values connected with the first two *exo*-effects were found to be: (i) in the temperature range of 157–293 °C; maximum at 198 °C, $\Delta H = -142$ J g^{-1} = -85.8 kJ mol^{-1} = -20.6 kcal mol^{-1}, (ii) in the temperature range of 299–360 °C; maximum at 350 °C, $\Delta H = -46.4$ J g^{-1} = -28.0 kJ mol^{-1} = -6.7 kcal mol^{-1}. The maximum of the third *exo*-effect is lying at 415 °C as was determined from DTA curve. The energy value connected with this degradation step was estimated to be $\Delta H = -2664$ J g^{-1} = -1609.1 kJ mol^{-1} = -385.9 kcal mol^{-1}. The thermal decay is finished at ca. 600 °C. The product of the thermal decomposition was identified by means of ^{57}Fe Mössbauer spectroscopy as α-Fe$_2$O$_3$ (i.e. hematite, $\delta = 0.37$ mm s^{-1}, $\varepsilon_Q = -0.21$ mm s^{-1}, $B_{HF} = 51.3$ T) the total weight loss found/calcd: 87.7%/87.3%.

3.6. DFT calculations

Preliminary geometry optimizations were performed on the HF/6-31* level. Then, geometries of Fe-complexes were fully optimized on the B3LYP level using the 6-311+G* basis set. Harmonic frequency analysis was used to verify the nature of founded stationary points as the minima. All calculations were performed using the Gaussian03 program package.[26] As a model compound, the complex involving N6-(benzyl)adenosine moiety (L_0) has been chosen for the calculations. According to experimental observations, attributes of all possible geometric, oxidation, and spin states have been investigated. Important structural parameters in the vicinity of the iron atom are summarized in Table 4. Optimized molecular structures are depicted in Figures 6 and 7.

The above-discussed Mössbauer and magnetic features clearly confirmed the presence of geometric, valence, and spin states within the Fe-complexes. As for the Fe^{III} compounds, two possible arrangements of the coordination sphere and compositions were found by interpreting the results of DFT calculations: (i) [Fe^{III}(L_0)Cl$_3$] with the tetrahedral geometry and 5/2 spin state (Fig. 6a, Table 4), (ii) [Fe^{III}(L_0)Cl$_3$(H$_2$O)] with the trigonal-bipyramidal geometry and 3/2 spin state (Fig. 6b, Table 4). The calculated Fe–Cl, Fe–N and Fe–O bond lengths correspond well to those found for similar systems as determined by single crystal X-ray analysis (see Table 4).[15]

Table 4
Selected interatomic parameters (Å, °) of the studied complexes calculated on the B3LYP/6-311+G* level

	Fe^{III} $S = 5/2$ (T_d)	Fe^{III} $S = 3/2$ (TB)	Fe^{II} $S = 4/2$ (T_d)	Fe^{II} $S = 2/2$ (TB)	Fe^{III} [a]	Fe^{II} [a]
Fe—Cl1	2.195	2.270	2.298	2.376	2.259[b], 2.310[c]	2.392[b], 2.433[c]
Fe—Cl2	2.207	2.242	2.367	2.372		
Fe—Cl3	2.196	2.298	2.269	2.361		
Fe—N	2.081	1.955	2.237	2.007	2.106[b], 2.194[c]	2.182[b], 2.234[c]
Fe—O	–	1.997	–	2.023	2.101[c]	2.135[c]
Cl1—Fe—Cl2	112.48	123.45	107.61	114.35		
Cl1—Fe—Cl3	113.97	121.91	128.97	124.11		
Cl2—Fe—Cl3	114.31	113.72	120.57	121.04		
N—Fe—Cl1	104.72	90.56	94.61	90.49		
N—Fe—Cl2	105.52	93.37	95.24	92.46		
N—Fe—Cl3	104.62	95.80	96.68	93.95		
Cl1—Fe—O	–	85.34	–	86.32		
Cl2—Fe—O	–	91.46	–	92.61		
Cl3—Fe—O	–	83.81	–	84.47		
N—Fe—O	–	174.87	–	174.79		

[a] The values represent mean values which were determined from known X-ray structures of complexes bearing [b]FeCl$_3$N or [c]FeCl$_3$NO chromophore and are deposited within the Cambridge Crystallographic Data Centre (CSD). T_d, tetrahedron; TB, trigonal-bipyramid.
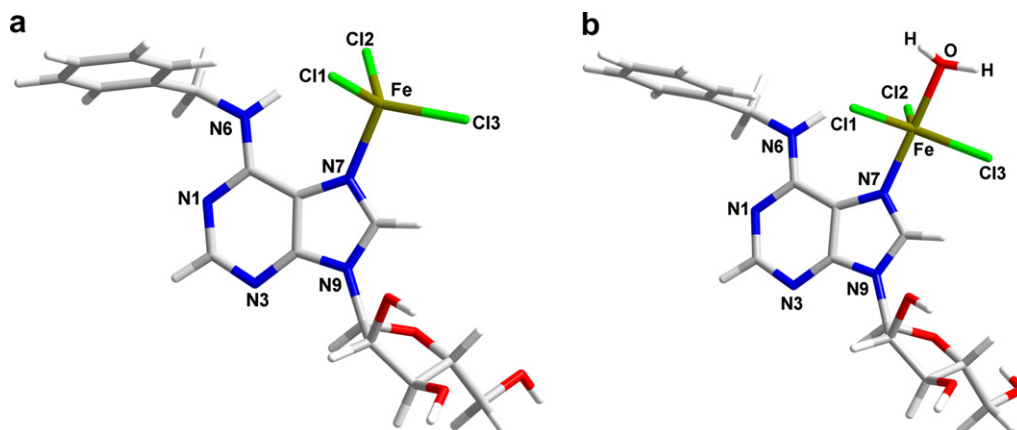

Figure 6. Geometries of [Fe^{III}(L_0)Cl$_3$] ($S = 5/2$) and [Fe^{III}(L_0)Cl$_3$(H$_2$O)] ($S = 3/2$) complexes optimized on the B3LYP/6-311+G* level.
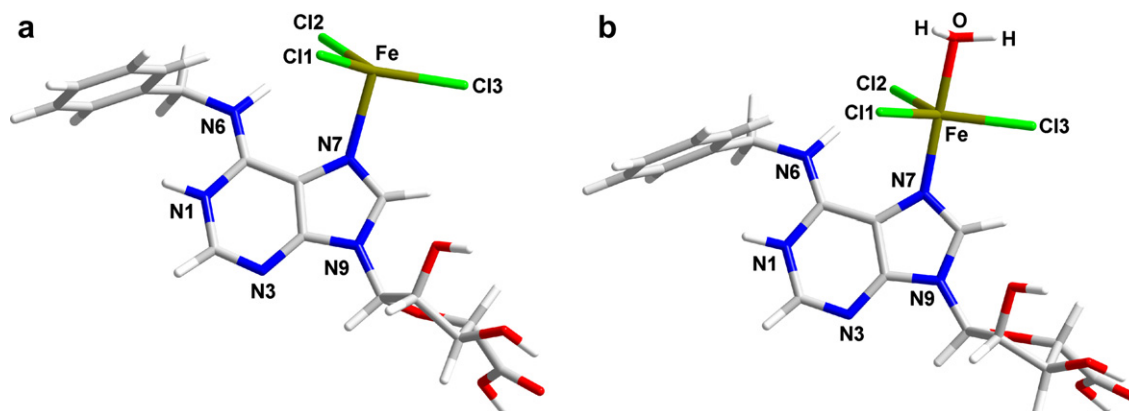
Figure 7. Geometries of $[Fe^{II}(H^+L_0)Cl_3]$ ($S = 4/2$) and $[Fe^{II}(H^+L_0)Cl_3(H_2O)]$ ($S = 2/2$) complexes optimized on the B3LYP/6-311+G* level.

Table 5
Selected IC_{50} (µM) values assessed by a calcein AM assay

Compound	IC_{50} (µM)			
	G-361	HOS	K-562	MCF-7
$[Fe(L_2)Cl_3] \cdot H_2O$ (**2**)	>50	8	9	16
L_2	>50	>50	>50	>50
$[Fe(L_6)Cl_3] \cdot H_2O$ (**6**)	>50	>50	>50	4
L_6	>50	>50	>50	>50
$FeCl_3 \cdot 6H_2O$	>200	>200	>200	>200

L_2 = N6-(4-fluorobenzyl)adenosine; L_6 = N6-(4-trifluoromethoxybenzyl)-adenosine. The human cancer cell lines (G-361, malignant melanoma; HOS, osteogenic sarcoma; K-562, chronic myelogenous leukemia; MCF-7, breast adenocarcinoma) were treated with the solution of the tested compound in the 0.5–50 µM range for 72 h, except for $FeCl_3 \cdot 6H_2O$, where the concentration range of 0.5–200 µM was used.

Similarly as for Fe^{III} complexes, two different geometries and spin states were found in the case of Fe^{II} components: (i) $[Fe^{II}(H^+L_0)Cl_3]$ – a deformed tetrahedral geometry with $S = 4/2$ (Fig. 7a, Table 4), (ii) $[Fe^{II}(H^+L_0)Cl_3(H_2O)]$ – a trigonal-bipyramidal geometry with $S = 2/2$ (Fig. 7b, Table 4). Besides, a protonation at the N1 or N3 position may occur in the case of Fe^{II} species. This fact can be connected with the oxidation of ribose simultaneously releasing a proton, and moreover, with the tautomeric shift of such a proton within the adenosine moiety. It has been found that the system with the ligand protonized at the N1 position is more stable as compared to the N3-protonized one. The calculated electronic energies were found to be lower by 11.70 and 11.94 kcal mol^{-1} in favor of the N1-protonated tautomer for tetrahedral and trigonal-bipyramidal arrangement, respectively. We may conclude that Fe^{II}–donor atom bond lengths are elongated in most cases in comparison with those calculated for Fe^{III} complexes, which is in good agreement with X-ray data published recently for complexes involving the same donor set (see Table 4).[15]

3.7. Biological activity testing

The selected results of in vitro cytotoxicity testing are listed in the Table 5. The cytotoxicity of the complexes, as well as of the starting compounds, was tested against the following human cancer cell lines: malignant melanoma (G-361), osteogenic sarcoma (HOS), chronic myelogenous leukemia (K-562), and breast adenocarcinoma (MCF-7). All free N6-(benzylamino)adenosine derivatives (L_1–L_7), used as ligands, showed cytotoxicity with IC_{50} > 50 µM, and $FeCl_3 \cdot 6H_2O$ even above 200 µM. The complex **2** showed significant cytotoxicity against the HOS, K-562, and MCF-7 cell lines, respectively (see Table 5). Moreover, a considerable

cytotoxicity has been found for the complex **6** on the MCF-7 cell line. These values are quite comparable to those found for cisplatin or oxaliplatin in the case of the same cell lines.[27] All the remaining complexes were found to be inactive within the evaluated concentration interval, and their IC_{50} values are higher than 50 µM. In conclusion, we may state that the complex formation had significant impact on the cytotoxicity results in the case of the complexes **2** and **6**, although the complexes have been characterized as mixtures from structural, valence, and spin-state point of view.

References and notes

1. Skoog, F.; Hamzi, H. G.; Szweykowska, A. M.; Leonard, N. J.; Carraway, K. L.; Fujii, T.; Helgeson, J. P.; Loeppky, R. N. *Phytochemistry* **1967**, *6*, 1169.
2. Raynaud, F. I.; Whittaker, S. R.; Fischer, P. M.; McClue, S.; Walton, M. I.; Barrie, S. E.; Garrett, M. D.; Rogers, P.; Clarke, S. J.; Kelland, L. R.; Valenti, M.; Brunton, L.; Eccles, S.; Lane, D. P.; Workman, P. *Clin. Cancer Res.* **2005**, *11*, 4875.
3. Maloň, M.; Trávníček, Z.; Maryško, M.; Zbořil, R.; Mašláň, M.; Marek, J.; Doležal, K.; Rolčík, J.; Kryštof, V.; Strnad, M. *Inorg. Chim. Acta* **2001**, *323*, 119.
4. Maloň, M.; Trávníček, Z.; Maryško, M.; Zbořil, R.; Mašláň, M.; Marek, J.; Doležal, K.; Holub, J.; Rolčík, J.; Strnad, M. *Transition Met. Chem.* **2002**, *27*, 580.
5. Trávníček, Z.; Maloň, M.; Zatloukal, M.; Doležal, K.; Strnad, M.; Marek, J. *J. Inorg. Biochem.* **2003**, *94*, 307.
6. Trávníček, Z.; Klanicová, A.; Popa, I.; Rolčík, J. *J. Inorg. Biochem.* **2005**, *99*, 776.
7. Mikulski, C. M.; Cocco, S.; De Franco, N.; Moore, T. *Inorg. Chim. Acta* **1985**, *106*, 89.
8. Mikulski, C. M.; Minutella, R.; De Franco, N.; Karayannis, N. M. *Inorg. Chim. Acta* **1985**, *106*, L33.
9. Capparelli, M. V.; Goodgame, D. M. L.; Hayman, P. B.; Skapski, A. C.; Hathway, D. E. *FEBS Lett.* **1983**, *1632*, 241.
10. Karayannis, N. M.; Cronin, J. T.; Mikulski, C. M.; Pytlewski, L. L.; Labes, M. M. *J. Inorg. Nucl. Chem.* **1971**, *33*, 4344.
11. Mikulski, C. M.; Mattucci, L.; Weiss, L.; Karayannis, N. M. *Inorg. Chim. Acta* **1985**, *107*, 147.
12. Mikulski, C. M.; Kurlan, M. K.; Bayne, M.; Gaul, M.; Karayannis, N. M. *Inorg. Chim. Acta* **1986**, *123*, 27.
13. Karayannis, N. M.; Mikulski, C. M.; Speca, A. N.; Cronin, J. T. *Inorg. Nucl. Chem. Lett.* **1981**, *17*, 261.
14. Mikulski, C. M.; Fleming, J.; Fleming, D.; Karayannis, N. M. *Inorg. Chem.* **1972**, *11*, 2330.
15. Allen, F. A. *Acta Crystallogr., Sect. B: Struct. Sci.* **2002**, *58*, 380.
16. Capparelli, M. V.; Goodgame, D. M. L.; Hayman, P. B.; Skapski, A. C. *Inorg. Chim. Acta* **1986**, *125*, L47.
17. Schmale, H. W.; Gyr, E.; Dubler, E. *Acta Crystallogr., Sect. C: Cryst. Struct. Commun.* **2000**, *56*, 957.
18. Boča, R.; Baran, P.; Dlháň, L.; Šima, J.; Wiesinger, G.; Renz, F.; El-Ayaan, U.; Linert, W. *Polyhedron* **1997**, *16*, 47.
19. Kahn, O. *Molecular Magnetism*; Wiley–VCH: New York, 1993.

20. Geary, W. J. *Coord. Chem. Rev.* **1971**, *7*, 81.
21. Doležal, K.; Popa, I.; Zatloukal, M.; Lenobel, R.; Hradecká, D.; Vojtěšek, B.; Uldrijan, S.; Mlejnek, P.; Werbrouck, S.; Strnad, M. European Patent Office, FR. (WO2004058791), **2004**.
22. Pouchert, C.J. *The Aldrich Library if Infrared Spectra (Edition III)*; Aldrich Chemical: 1001 W. St. Paul. Ave., Milwukee, Wisconsin, 53233, 1981.
23. Fujita, T.; Sakaguchi, T. *Chem. Pharm. Bull.* **1977**, *25*, 2419.
24. Nakamoto, K. *Infrared and Raman spectra of Inorganic and Coordination Compounds*; Wiley: New York, 1997.
25. Sreekanth, A.; Prathapachandra Kurup, M. R. *Polyhedron* **2004**, *23*, 969.
26. Frisch, M.J.; Trucks, G.W.; Schlegel, H.B.; Scuseria, G.E.; Robb, M.A.; Cheeseman, J.R.; Montgomery, Jr., J.A.; Vreven, T.; Kudin, K.N.; Burant, J.C.; Millam, J.M.; Iyengar, S.S.; Tomasi, J.; Barone, V.; Mennucci, B.; Cossi, M.; Scalmani, G.; Rega, N.; Petersson, G.A.; Nakatsuji, H.; Hada, M.; Ehara, M.; Toyota, K.; Fukuda, R.; Hasegawa, J.; Ishida, M.; Nakajima, T.; Honda, Y.; Kitao, O.; Nakai, H.; Klene, M.; Li, X.; Knox, J.E.; Hratchian, H.P.; Cross, J.B.; Bakken, V.; Adamo, C.; Jaramillo, J.; Gomperts, R.; Stratmann, R.E.; Yazyev, O.; Austin, A.J.; Cammi, R.; Pomelli, C.; Ochterski, J.W.; Ayala, P.Y.; Morokuma, K.; Voth, G.A.; Salvador, P.; Dannenberg, J.J.; Zakrzewski, V.G.; Dapprich, S.; Daniels, A.D.; Strain, M.C.; Farkas, O.; Malick, D.K.; Rabuck, A.D.; Raghavachari, K.; Foresman, J.B.; Ortiz, J.V.; Cui, Q.; Baboul, A.G.; Clifford, S.; Cioslowski, J.; Stefanov, B.B.; Liu, G.; Liashenko, A.; Piskorz, P.; Komaromi, I.; Martin, R.L.; Fox, D.J.; Keith, T.; Al-Laham, M.A.; Peng, C.Y.; Nanayakkara, A.; Challacombe, M.; Gill, P.M.W.; Johnson, B.; Chen, W.; Wong, M.W.; Gonzalez, C.; and Pople, J.A.; Gaussian 03, Revision C.02, Gaussian, Inc., Wallingford CT, 2004.
27. Trávníček, Z.; Szücová, L.; Popa, I. *J. Inorg. Biochem.* **2007**, *101*, 477.